Atmospheric Research 182 (2016) 269–281

Contents lists available at ScienceDirect

Atmospheric Research

journal homepage: www.elsevier.com/locate/atmosres

A multi-sensor study of the impact of ground-based glaciogenic seeding on clouds and precipitation over mountains in Wyoming. Part I: Project description

Binod Pokharel *, Bart Geerts

Department of Atmospheric Science, University of Wyoming, Laramie, Wyoming 82071, USA

ARTICLE INFO

Article history:
Received 4 May 2016
Received in revised form 4 August 2016
Accepted 8 August 2016
Available online 13 August 2016

Keywords:
Glaciogenic seeding
Orographic cloud and precipitation
Radar reflectivity
Airborne measurements

ABSTRACT

The AgI Seeding Cloud Impact Investigation (ASCII) campaign was conducted in early 2012 and 2013 over two mountain ranges in southern Wyoming to examine the impact of ground-based glaciogenic seeding on snow growth in winter orographic clouds. The campaign was supported by a network of ground-based instruments, including microwave radiometers, two profiling Ka-band Micro-Rain Radars (MRRs), a Doppler on Wheels (DOW) X-band radar, and a Parsivel disdrometer. The University of Wyoming King Air operated the profiling Wyoming Cloud Radar, the Wyoming Cloud Lidar, and in situ cloud and precipitation particle probes. The characteristics of the orographic clouds, flow field, and upstream stability profiles in 27 intensive observation periods (IOPs) are described here. A composite analysis of the impact of seeding on snow growth is presented in Part II of this study (Pokharel et al., 2017).

Clouds were stratiform in most IOPs, but in 10 IOPs convective clouds were present. Most clouds were shallow (~2 km deep), all had some liquid water but generally with a liquid water path <0.3 mm, and all were naturally precipitating but generally at a rate <1 mm h^{-1}.

1. Introduction

A significant amount of precipitation in arid mid-latitude regions such as the western USA falls as snow over mountains in winter. The resulting snowpack serves as a natural reservoir controlling the stream flow of some major rivers such as the Colorado River, which is the main source of water for the arid southwestern US. Therefore there has been much interest in methods to enhance the snowpack in this region. The most common method, used for more than half a century, is to seed orographic clouds glaciogenically, mostly using silver iodide (AgI).

Orographic clouds almost always contain supercooled liquid water (SLW) at temperatures above −20 °C and often colder (Huggins, 1995; Rauber and Grant, 1987; Politovich and Vali, 1983), because natural ice nuclei are rare and because the condensate supply rate tends to exceed the diffusional growth rate of ice. Glaciogenic seeding intends to rapidly convert this SLW into frozen hydrometeors. The timing, location and amount of SLW are quite sensitive to atmospheric conditions (Rauber and Tokay, 1991; Sassen et al., 1990), in particular cloud base temperature, cross-mountain wind speed and terrain steepness. Slight variations in wind direction can alter the location of the maximum liquid water content (LWC).

Over the interior mountains in the western US, e.g. in Colorado and Wyoming, the LWC typically is quite low in mixed-phase clouds. Reported maximum LWC values at flight level are around 0.3 g m^{-3} (Cooper and Vali, 1981; Rogers and Vali, 1987; Politovich and Vali, 1983). Typically the mode of the drop size distribution is about 10–15 μm of diameter in winter orographic clouds in this region (Politovich and Vali, 1983; Cooper and Vali, 1981). The lack of larger drops implies that most snow growth is by vapor diffusion and aggregation, rather than accretion, because larger droplets (diameter larger than 20–30 μm) are required for the snow growth by riming (Pruppacher and Klett, 1997; Wang and Ji, 2000).

The basic requirement for effective glaciogenic seeding of an orographic cloud containing SLW is that the seeding material (in this case AgI nuclei) effectively disperses in a cloud in a temperature window between about −20 and −5 °C (Grant and Elliott, 1974). The lower threshold is based on the fact that natural ice nuclei become more abundant below ~−20 °C, depending mainly on the concentration of a large aerosol in the upstream airmass (diameter > 0.5 μm, DeMott et al., 2010). The upper threshold, around −8 to −5 °C, is the maximum activation temperature of AgI (DeMott et al., 1983; DeMott, 1997).

The AgI Seeding Cloud Impact Investigation (ASCII) campaign was conducted in early 2012 and 2013 over two mountain ranges in southern Wyoming. Most ASCII intensive observation periods (IOPs)

Abbreviations: ASCII, AgI Seeding Cloud Impact Investigation; UWKA, University of Wyoming King Air; WCR, Wyoming Cloud Radar; WCL, Wyoming Cloud Lidar; MRR, Micro-Rain Radar; DOW, Doppler on Wheels.

* Corresponding author.
E-mail address: bpokhare@uwyo.edu (B. Pokharel).

http://dx.doi.org/10.1016/j.atmosres.2016.08.008
0169-8095/

were conducted in post-frontal synoptic conditions. Deep frontal systems producing widespread precipitation were not targeted in ASCII for two reasons. Firstly, deep baroclinic systems have low cloud top temperatures (often below −20 °C) and thus are characterized by ice nucleation near the cloud top, often within small generating cells (Plummer et al., 2014), followed by diffusional growth and aggregation of ice particles during fallout to the surface (the "seeder–feeder" process; Hobbs, 1975; Rauber, 1987; Long and Carter, 1996; Cooper and Saunders, 1980). Secondly, such systems are rarely steady. Steadiness of flow, stability, and cloud and precipitation structure is needed in ASCII as an untreated period is compared to a treated period. Shallow orographic clouds can persist long after deep frontal disturbances have passed. They produce persistent light snowfall over mountains even from air containing relatively little SLW (e.g., Rauber, 1987; Pokharel and Geerts, 2014). Because of their persistence, shallow orographic clouds serve as a good natural laboratory for controlled experiments. These clouds are also good targets for glaciogenic seeding since snow growth may be inefficient, due to a scarcity of natural ice nuclei (cloud top temperatures typically are above −20 °C) and strong, SLW-producing updrafts.

In ASCII, glaciogenic nuclei were injected into the orographic flow by means of propane-burning generators on the ground. Ground-based cloud seeding outcomes do not only depend on cloud temperature, liquid water, and wind direction, but also on (1) the ability for the underlying earth surface to initiate ice crystals into the cloud, potentially overwhelming the effect of AgI seeding, and (2) the presence of boundary layer turbulence to mix the seeding material into the cloud. These two processes are important and need to be considered in cloud seeding experiments. Regarding the first process, there is some evidence that ice crystals are naturally inserted into supercooled orographic clouds hugging the terrain (Rogers and Vali, 1987), through two mechanisms: the lofting of blowing snow (Geerts et al., 2015b), and ice multiplication by splintering as supercooled droplets impact rimed obstacles at the surface, such as trees (Geerts et al., 2011). Regarding the second process, boundary-layer turbulence is important not only to mix natural ground-initiated ice crystals or AgI nuclei into cloud, but possibly also to enhance snow growth in mixed-phase clouds (Geerts et al., 2011). Either process may explain why shallow orographic clouds coupled to the surface tend to be effective snow producers, more effective than elevated lenticular clouds over mountains for instance. Qualitative indicators are used in ASCII to judge the potential significance of these processes in ASCII: blowing snow requires fresh snow and strong surface winds, at least 10–12 m s^{-1} (Dery and Yau, 1999). The Hallett–Mossop ice multiplication process is rather sensitive to temperature ($-4 < T < -8$ °C between cloud base and mountain crest level) and droplet size (diameter > ~25 μm) (Harris-Hobbs and Cooper, 1987).

The concentration of a cloud-active aerosol (cloud condensation nuclei or ice nuclei) in the inflow can also affect the efficacy of orographic cloud seeding (e.g., Givati and Rosenfeld, 2005). That topic is beyond the scope of the ASCII objectives. No aerosol measurements were made in ASCII.

The objective of this study is to explore a seeding signal in the ASCII IOPs, in terms of ice crystal size distribution and mainly snowfall rate. This composite study complements a number of ASCII case studies (Pokharel et al., 2014a, b; Chu et al., 2014; Pokharel et al., 2015).

Before we can explore the impact of seeding, we first must describe the campaign design, and the flow, stability, and cloud characteristics during the ASCII IOPs. That is the topic of this paper (Part I). The ASCII experimental design and instruments are described in Section 2. The ambient atmospheric conditions observed in ASCII are described in Section 3. The radar-derived horizontal and vertical structure of ASCII storms is described in Section 4, and flight-level cloud and precipitation particles are characterized in Section 5. The correlation between control and target regions precipitation is discussed in Section 6 and a summary is given in Section 7. A companion paper (Pokharel et al., 2017, hereafter referred to as Part II) will explore the AgI seeding impact using radar and particle probe data.

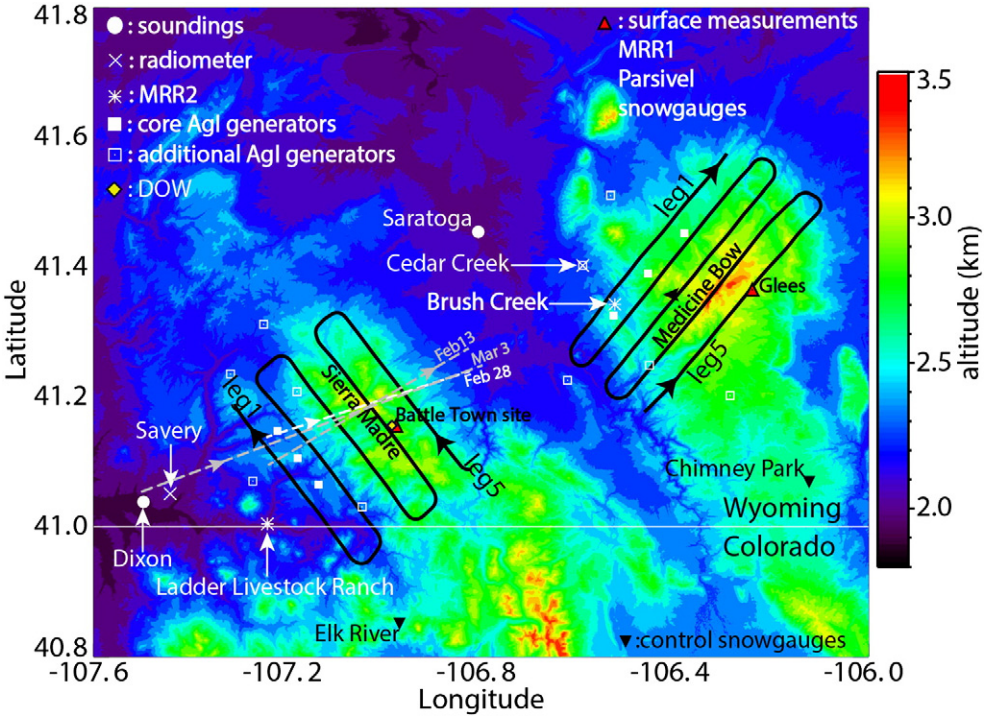

Fig. 1. ASCII experimental design map over the Sierra Madre (SM) and Medicine Bow (MB) mountains in southern Wyoming. The solid black lines show the UWKA flight tracks and square symbols show the ground-based AgI generators. The three most commonly used AgI generators are shown by the filled squares. Other symbols represent the various instrument locations. The dashed lines show the location of along-wind legs flown during three different IOPs. Data from these legs are shown below.

2. Experimental design

2.1. Field campaigns

The ASCII project was conducted during four winters. The largest field deployment, 'ASCII-12', ran from January to March of 2012 over the Sierra Madre (SM) (Fig. 1) (Geerts et al., 2013). A year later 'ASCII-13' was conducted over the Medicine Bow (MB) mountains (Pokharel and Geerts, 2014). In addition, small campaigns were conducted over the MB in early 2008 and early 2009, collectively called 'pre-ASCII'. Pre-ASCII laid the groundwork for ASCII and was rather small, deploying an aircraft and soundings only, but the flight tracks, their sequence, and seeding operations were exactly the same as in ASCII-13.

All three ASCII campaigns were conducted in the context of the Wyoming Weather Modification Pilot Project (WWMPP, Breed et al., 2014), a multi-year randomized seeding experiment (RSE). WWMPP targeted both mountain ranges (SM and MB) randomly, switching on eight AgI generators for 4 h over *either* mountain, when pre-defined criteria were met over *both* mountains. These criteria address temperature ($T_{700\ mb} < -8$ °C), wind direction (between 225° and 315°), and liquid water presence according to radiometer data, the latter sometimes substituted by the presence of visual clouds (Breed et al., 2014). The ASCII IOPs are mostly separate from the RSE cases because ASCII has somewhat different case calling criteria (Section 3), in particular requiring steady conditions, to contrast a treated against an untreated period in each individual case. Also, ASCII IOPs employ just three AgI generators (filled squares in Fig. 1), aligned roughly normal to the low-level wind. The purpose is to contrast an upwind control region against a target region over the same mountain, and to examine changes in seeding impact with fetch. A few IOPs are joint ASCII-RSE cases (three in ASCII-12 and two in ASCII-13); in these IOPs all eight generators are used. These five IOPs do not afford a lateral control region nor fetch-dependent analysis.

2.2. Instruments and measurements

All three ASCII field deployments involved the University of Wyoming King Air (UWKA) with the Wyoming Cloud Radar (WCR). The WCR is a W-band (3 mm) profiling (above and below flight level) Doppler radar, with dual-Doppler capability below flight level (Geerts et al., 2006). The UWKA also operated an array of cloud and precipitation probes, and the profiling Wyoming Cloud Lidar (WCL) (Wang et al., 2012). The UWKA operated a Cloud Droplet Probe (CDP) with 31 bins between 2.5 and 50 μm, and two optical array probes, a Cloud Imaging Probe (CIP) and a 2-D precipitation probe (2DP). The CIP has 101 bins between 13 and 2500 μm, but concentrations in the first two bins are ignored because they are less reliable. The 2DP has 101 bins between 0.1 and 20 mm.

Table 1
Summary of all 27 ASCII IOPs. The SEED and NOSEED times are specific to UWKA flight data. For ground-based instruments, the corresponding times are shown in Fig. 2. "mtn" is the target mountain (MB = Medicine Bow, SM = Sierra Madre); "nn" is the number of AgI generators in operation during SEED. The different variables given in this table are derived from rawinsonde released from Saratoga (ASCII-13 and pre-ASCII) and from Dixon (ASCII-12) (Fig. 1) during the IOPs. The lifting condensation level (LCL) is based on sounding data, mixed adiabatically between 100 and 500 m AGL. (The lowest 100 m of sounding data are ignorEd.) The Brunt–Vaisala frequency (N) is the dry (moist) value below (above) the cloud base (LCL). The Froude number (Fr) is calculated as the wind speed divided by N and by the height of the mountain's peak above the sounding site. The wind speed and direction are computed from the average wind vector between the near-surface and mountain top level. α is the angle between this wind direction and the line normal to the flight tracks (309° for the MB and 226° for the SM); α is positive when the wind blows from a direction clockwise of the normal line. The mean cloud depth is calculated as the vertical distance between the LCL and the WCR echo top (−20 dBZ) height averaged over all legs and ladders. The liquid water path (LWP) is measured by an upstream radiometer (Fig. 1). The convective (CONV) and stratiform (STRF) cloud types are defined based on reflectivity and vertical velocity patterns in WCR transects, and from DOW reflectivity if no WCR data are available. The rows in italics indicate IOPs without UWKA flight.

Date	mtn	Time (UTC)						nn	700 mb T	Cloud base (LCL)		Average value from surface to mountain top					Mean cloud depth	Radio-meter mean LWP	Cloud type	Is flight level in-situ data used?
		UWKA NOSEED		UWKA SEED		AgI generators				T	Altitude	N	Fr	Wind speed	Wind dir	α				
		Start	End	Start	End	Start	End	_	°C	°C	m MSL	10^{-2} s^{-1}	–	m s^{-1}	deg	deg	km	mm		
11-Jan.-13	MB	2246	2412	2618	2740	2600	2800	8	−17	−16.7	2781	0.56	1.73	14.5	268	−41	1.3	0.1	CONV	No
16-Jan.-13	MB	0009	0300	0210	0338	0128	0229	3	−13.4	−13.1	2764	1.69	0.40	10	269	−40	1.5	0.13	STRF	Yes
29-Jan.-13	MB	2159	2324	2405	2536	2315	2516	3	−16.1	−13.7	2598	0.42	0.97	6.4	338	29	2.3	0.04	STRF	Yes
1-Feb.-13	MB	1903	2028	2029	2155	2023	2423	8	−8	−6	2785	0.94	1.57	20.2	277	−32	2.4	0.43	STRF	No
13-Feb.-13	MB	0150	0402	0404	0523	0315	0515	2	−12.4	−12.2	2972	1.36	0.47	9.6	254	−55	0.6	0.07	STRF	No
18-Feb.-13	MB	1556	1755	1800	1925	1713	1913	2	−14.3	−15.2	3071	0.68	1.36	14.4	283	−26	1.5	0.15	CONV	Yes
1-Mar.-13	MB	0039	0207	0246	0411	0156	0407	3	−10	−9.8	3008	0.9	1.11	16	297	−12	1.5	0.22	CONV	Yes
1-Mar.-13	MB	2010	2210	2217	2343	1959	2357	3	−6.5	−4	2859	0.79	1	12.9	298	−11	1.9	0.14	STRF	Yes
11-Feb.-08	MB	2003	2123	2133	2249	2128	2328	3	−9.7	−13.2	2723	0.79	1.33	15.8	319	10	2.7	0.06	CONV	No
25-Feb.-08	MB	2029	2146	2220	2337	2155	2355	3	−8.9	−6.6	2759	0.31	2.65	12.6	295	−14	3.1	N/A	STRF	No
18-Feb.-09	MB	1644	1813	1834	1952	1812	2012	3	−10.3	−9.1	2743	0.76	1.19	14	304	−5	2.0	0.18	STRF	No
20-Feb.-09	MB	2154	2308	2332	2403	2320	2520	3	−10.1	−7.2	2452	0.77	1.3	15.6	309	0	4.1	0.06	STRF	No
10-Mar.-09	MB	1421	1453	1537	1749	1454	1654	3	−17.8	−17.4	2855	0.37	3.88	22	274	−35	1.2	0.03	CONV	No
25-Mar.-09	MB	1613	1644	1725	1928	1643	1843	3	−10.1	−8.8	2835	0.46	1.96	13.7	266	−43	3.3	0.12	CONV	No
30-Mar.-09	MB	1723	1755	1836	2013	1752	1952	3	−16.3	−14.1	2609	0.41	1.77	10.9	324	15	2.5	0.02	CONV	No
18-Jan.-12	SM	0025	0130	0206	0247	0130	0331	3	−6.3	−10.4	3593	0.92	1.68	19.5	240	14	1.8	0.085	STRF	Yes
19-Jan.-12	*SM*					*1811*	*2018*	*3*	*−2.6*	*−4.9*	*3331*	*0.87*	*1.72*	*18.9*	*237*	11		*0.15*	*STRF*	*N/A*
11-Feb.-12	*SM*					*0445*	*0750*	*8*	*−5.5*	*−1.9*	*2537*	*0.86*	*1.10*	*12.6*	*268*	42		*0.065*	*STRF*	*N/A*
12-Feb.-12	*SM*					*2300*	*0300*	*3*	*−6.0*	*−3.9*	*2471*	*1.08*	*1.48*	*7.7*	*279*	53		*0.022*	*CONV*	*N/A*
13-Feb.-12	SM	1922	2058	2100	2015	2015	2215	3	−8.2	−4.2	2418	0.32	1.61	5.1	249	23	1.4	0.026	CONV	Yes
14-Feb.-12	SM	2258	0034	0036	0139	0005	0205	3	−8.0	−4.9	2513	0.52	1.38	9.5	278	52	1.7	0.065	STRF	Yes
21-Feb.-12	SM	1957	2112	2143	2259	2120	0118	8	−8.4	−7.4	2917	0.68	1.76	15.9	251	25	1.9	0.218	STRF	No
22-Feb.-12	SM	1405	1519	1538	1637	1510	1710	3	−4.6	−3.2	2870	0.84	1.87	20.5	260	34	1.5	0.308	STRF	No
28-Feb.-12	SM	1358	1520	1521	1625	1504	1700	3	−7.2	−3.1	2336	0.34	3.02	12.9	240	14	5.8	0.173	STRF	Yes
28-Feb.-12	SM	1951	2103	2121	2234	2056	2300	3	−9.1	−6.5	2624	0.27	5.06	15.3	280	54	2.4	0.073	CONV	Yes
29-Feb.-12	SM	0158	0310	2254	2407	2130	0000	3	−7.7	−8.0	3012	0.49	3.03	18.3	213	−13	1.6	0.116	STRF	Yes
03-Mar.-12	SM	1816	1932	2000	2116	1930	2330	8	−11.4	−9.1	2767	0.72	2.06	14.6	266	40	1.2	0.08	STRF	No

A geographically fixed "ladder" (or lawnmower) pattern with five tracks (Fig. 1) was flown twice without any seeding and then twice with the AgI generators in operation. One flight track upwind of the generators serves as upwind control (leg 1 in Fig. 1) and the four other tracks serve as target (legs 2–5 in Fig. 1). The ladders were flown from leg 5 (lee side) to leg 1 (upwind side) to avoid contamination by APIPs (aircraft-produced ice particles).

At least three (one) rawinsondes were released from upstream of the target mountain in each ASCII-12 (ASCII-13 and pre-ASCII) IOP, i.e. from Dixon in ASCII-12, and from Saratoga in ASCII-13 and pre-ASCII (Fig. 1). Supercooled liquid water was monitored by a passive microwave radiometer located upstream of the target mountains, and pointed towards the mountain at an elevation angle just above the terrain (Fig. 1).

The ASCII-12 campaign included an array of instruments on the ground (Geerts et al., 2013), including a dual-polarization scanning X-band (3 cm) Doppler-on-Wheels (DOW) radar, two profiling Ka-band (1.2 cm) Micro Rain Radars (MRRs), a Parsivel disdrometer, a Cloud Particle Imager (CPI), snow gauges, and surface weather stations (Fig. 1). The ASCII-13 instrument array was sparser (Pokharel and Geerts, 2014); in particular, it did not include a DOW. In some ASCII-13 cases there was no snowfall at the target site, which was somewhat unfortunately located in the lee of Medicine Bow Peak, behind a steep escarpment. Several ASCII-13 cases were so shallow that the snowfall occurred almost exclusively on the upwind side. These conditions limited the data from surface measurements in ASCII-13.

Freshly fallen snow was collected regularly in most ASCII-12 IOPs for trace element analysis, including Ag, to confirm that the seeding plume extended over the target site. There was no independent measurement of the dispersal of AgI plumes, e.g. by the release of a trace gas from the AgI generators. Thus we estimate the extent of the AgI plumes based on proximity wind direction (sounding data) and an assumed plume width. As discussed in Part II, the assumed plume width is based on direct airborne measurements of AgI nuclei over the MB in a separate campaign in 2011 (Boe et al., 2014), and on associated numerical modelling (Xue et al., 2014).

The UWKA aircraft in situ cloud probes are used mainly to characterize liquid and frozen particle size distributions and LWC. They are less useful for the purpose of ground-based seeding signature detection, as

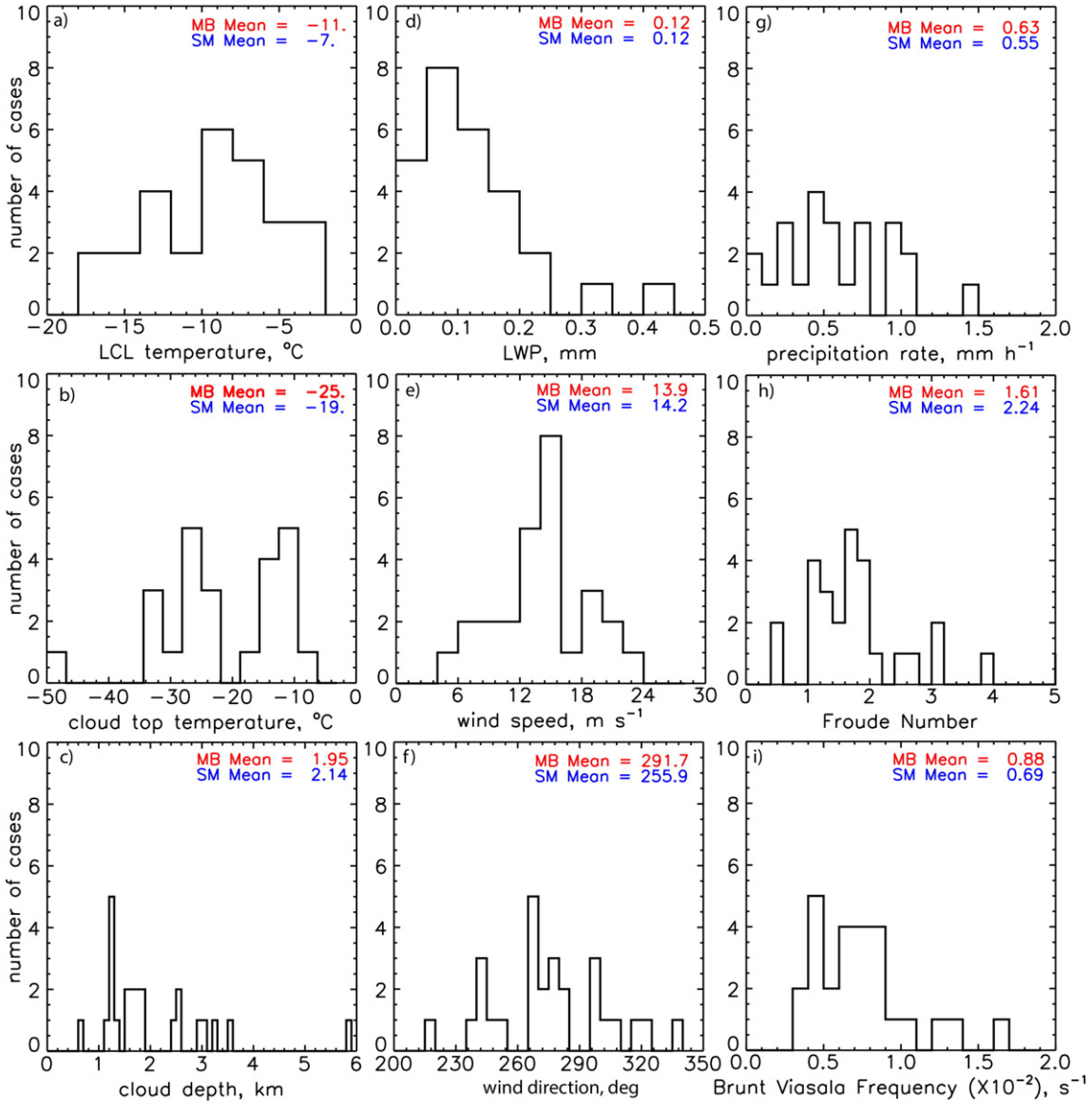

Fig. 2. Distribution of different atmospheric parameters during the 24 ASCII IOPs with WCR data. The average values over the two mountains (MB and SM) are shown in the upper right of each panel. a) LCL temperature, from soundings; b) cloud top temperature from the WCR echo top height and soundings; c) cloud depth; d) liquid water path (LWP) measured by the upstream microwave radiometer; e) average wind speed from the upstream valley floor to the mountain top, from soundings; f) precipitation rate calculated from the average WCR reflectivity at low level (surface to 500 m AGL) using the Z/R relationship; g) Froude number, from soundings; and h) stability parameter (Brunt Vaisala frequency (N)), from soundings.

the flight level (usually the lowest allowed by flight regulations, i.e. 610 m above the highest terrain) generally is too high to sample boundary layer air. Also, some in-situ probes became iced over by accreting SLW in some IOPs. On some flights the flight level was raised to avoid aircraft icing, making the in situ measurements less relevant. But no matter what flight level, the WCR nadir antenna provides data within ~30 m of the ground. The ability to detect changes near the ground is important because of ground-based seeding and the shallowness of ASCII clouds.

3. Ambient atmospheric conditions and cloud characteristics in ASCII

3.1. IOP initiation criteria

For IOP-calling purposes, ASCII used a temperature criterion (upper threshold only), a basic wind direction criterion (to ensure that the AgI plumes are advected towards the instrumented target region), a cloud criterion (IOPs are started only in the presence of a visual cloud over the mountain and/or of liquid water as measured by a radiometer), and a wind speed plus stability criterion (to ensure that the upstream airmass can be lifted over the mountain barrier, rather than be trapped or deflected). The actual values for all these parameters during each IOP are listed in Table 1. In addition, relatively steady conditions were required for at least 4 h, to allow a comparison between untreated and treated periods. This assessment was based on output from a real-time 4D data assimilation and high-resolution (2 km) numerical simulation, updated frequently as part of the WWMPP (Breed et al., 2014). IOPs were called for only if no significant changes were anticipated in the low-level flow, stability, and precipitation rate. In fact two IOPs are excluded from this study because the data reveal a wind shift and/or temperature drop indicative of the passage of a front or mesoscale disturbance during the IOP. The ASCII case calling criteria were more flexible compared to the WWMPP. For example, ASCII-12 includes several IOPs with a 700 mb temperature warmer than −8 °C (Table 1), the threshold used for the WWMPP (Breed et al., 2014). (The 700 mb level roughly corresponds with the height of Battle Pass in the SM.) The warmer IOPs were called for only if there was evidence that AgI could be mixed over a sufficient depth, by wind-driven turbulence or convection.

3.2. Upstream stability and flow conditions

A total of 27 good IOPs resulted from the ASCII campaigns (Table 1). Of these, 24 IOPs include UWKA measurements while three (all in ASCII-12) only have ground-based measurements. 15 IOPs were conducted over the MB, and 12 over the SM. The experiment was conducted in a variety of atmospheric and cloud conditions (Table 1). The “SEED” (“NOSEED”) period in Table 1 refer to the period of UWKA measurements over the target and control tracks, with the AgI generators on (off). Generally the SEED period follows the NOSEED period, separated by an ~30 min buffer period, which in most cases is long enough for the AgI nuclei to be advected across the target tracks. For some low-wind IOPs the SEED period is reduced to account for the delayed arrival time of the AgI plume. The advection time is estimated based on the average wind speed and direction between the surface and mountain top level, listed in Table 1. One or two along-wind legs were flown during the buffer period, to examine the cloud and precipitation structure in a transect across the mountain.

Most ASCII IOPs took place well after the passage of a frontal system, with a stable layer slightly above mountain top level, resulting in

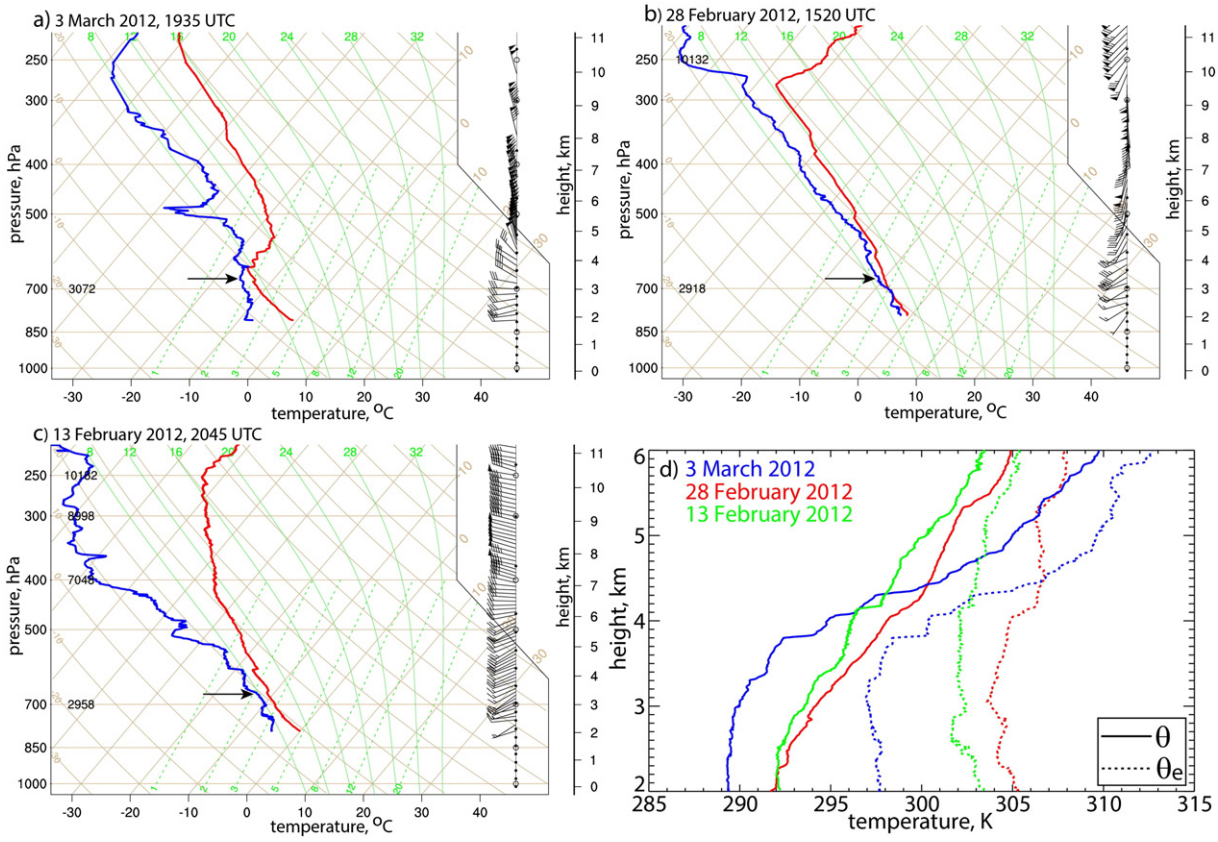

Fig. 3. An example of vertical profiles of upstream atmospheric conditions during ASCII, obtained from radiosondes released from Dixon (Fig. 1) during ASCII-12. (a–c) Skew-T logP displays. The black arrow in each sounding indicates mountain top height. A full barb equals 5 m s^{-1} (~10 kts). d) Vertical profiles of potential temperature θ and equivalent potential temperature θ_e for the soundings in (a–c).

shallow orographic clouds. Deep orographic clouds were present only in a few cases. Some examples are shown below.

Fig. 2 shows the diversity of atmospheric and cloud conditions during the 24 ASCII IOPs with WCR data. The ASCII IOPs span a rather large range of cloud base (or lifting condensation level, LCL) temperatures (−2 to −18 °C) and cloud top temperatures (−8 to −50 °C), but in general clouds are rather shallow (~2 km), the liquid water path (LWP) low (<0.2 mm), and the snowfall rate light (<1 mm h^{-1}). In some IOPs the cloud tops are near the shallow, post-frontal tropopause, but clouds are never deeper than 6 km. In most cases the clouds are purely orographic, i.e. clear air is present both upwind and downwind of the target mountain. Ice-free supercooled stratus or stratocumulus clouds of the type targeted in very early cloud seeding experiments (e.g., Schaefer, 1946) are not encountered in ASCII. The low-level wind speed generally is high, but varies significantly from case to case (Table 1). Winds weaker than 10 m s^{-1} occur in just three cases (Fig. 2e). The low-level B–V frequency varies much, but is generally low (<1×10^{-2} s^{-1}). As a result of the high wind and the low stratification, the Froude number (*Fr*) is generally high (*Fr* > 1 in all but two cases) (Table 1), and thus the flow is expected to move across the mountain and thus over the target region. The IOPs over the MB are generally colder than those over SM, with lower cloud base and cloud top temperatures (Fig. 2a and b). The wind direction is mostly southwesterly in the SM, and mostly northwesterly during the IOPs over the MB (Fig. 2f), by design (Section 3.1): to ensure that the AgI plumes would advect towards the target area, ASCII IOPs were only initiated when a significant component of the low-level wind was normal to the flight legs and terrain ridgeline (Fig. 1). This was the case in most IOPs, but not all, with a maximum departure of 55° from normal (Table 1).

In short, the array of clouds targeted in ASCII includes shallow to moderately deep orographic clouds, with a broad range of cloud base/top temperatures, wind speeds, supercooled liquid water content, ice crystal concentration, and cloud depths.

4. Structure of orographic clouds and precipitation in ASCII

Cloud types sampled during ASCII can be grouped in two types: stratiform only, and containing convection. The classification is based on WCR vertical velocity, and on DOW and/or WCR reflectivity texture. Convective IOPs are identified as those whose WCR transects reveal narrow updrafts with peak WCR vertical velocity exceeding 1.0 m s^{-1}. The threshold value (1.0 m s^{-1}) is arbitrary, and intended to ensure that some hydrometeors are carried upward before falling down to earth (Houze, 2014). At the same time, DOW low-level reflectivity maps (if available, i.e. in ASCII-12) reveal highly delineated patches of rather high reflectivity, either isolated or embedded in weak (stratiform) echoes. WCR reflectivity transects (and if available, DOW RHIs) should reveal the same convective echo structure. In most shallow convective IOPs, cumuliform cloud tops are evident also visually, from the flight deck. Finally, these (subjective) criteria have to persist for most of the duration of the IOP. Other IOPs are stratiform. Stratiform IOPs may witness strong updrafts (including WCR vertical velocity exceeding 1.0 m s^{-1}), especially under strong winds, but they lack the convective texture. Examples are given below.

Nearly two thirds of the ASCII IOPs have only stratiform clouds (Table 1). Stratiform clouds produce steady precipitation, mostly falling upwind of the mountain crest (Jing et al., 2015). Plunging flow in the lee is commonly observed in stratiform cloud conditions (Geerts et al.,

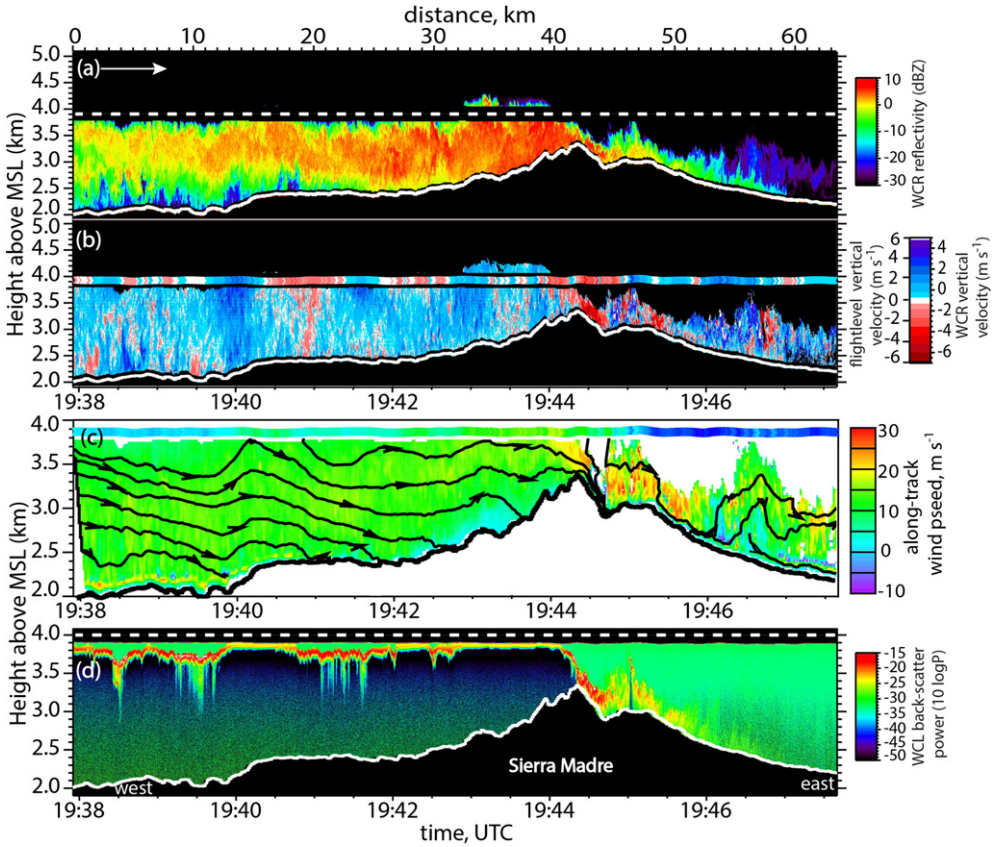

Fig. 4. WCR and WCL transect for the along-wind flight leg over the SM range on 3 March 2012 shown in Fig. 1. The wind direction and UWKA flight is from left (west) to right (east). a) WCR reflectivity; b) WCR hydrometeor vertical velocity profile; also shown, at flight level, is the gust probe air vertical velocity; c) WCR dual-Doppler synthesized along-track horizontal wind below flight level and hydrometeor streamlines (black lines with arrow); also shown, at flight level, is the gust probe along-track wind speed; and d) WCL backscatter power below flight level. The dashed white line in panels (a) and (c) is the UWKA flight level, and the white line below is the terrain profile. The WCR vertical velocity scale is offset by 1 m s^{-1} to account for the typical fallspeed of unrimed snow. Thus blue (red) regions in panel (b) can be interpreted as updrafts (downdrafts).

2015a). The remaining 10 ASCII IOPs are convective. In these cases natural precipitation tends to fall predominantly in the lee, and plunging flow is less common (Geerts et al., 2015a; Jing and Geerts, 2015). In several IOPs the clouds are no more than boundary-layer convection, topping out at <2 km deep AGL.

We now illustrate these two cloud types by means of three transects of WCR and WCL data, plus low-elevation DOW maps. In each case, the flight track (shown in Fig. 1) is approximately along the low-level wind. The upstream sounding for each case is shown in Fig. 3.

4.1. Stratiform clouds

The first example is a shallow stratiform cloud observed on 3 March 2012 (Fig. 4). Corresponding DOW reflectivity and radial velocity maps are found in Fig. 5a–b. Because the DOW is located in a saddle on the SM crest (Battle Pass, Fig. 1), there is no low-level DOW coverage to the NW and SE along the terrain crest (Jing et al., 2015). The corresponding sounding for this transect (Fig. 3a) shows a shallow cloud layer capped by a deep stable layer just above mountain top level, and low-level wind from the west, veering with height across the inversion. The average low-level wind is quite strong (15 m s^{-1}, Table 1), resulting in flow that readily ascends the SM range (Fr ~ 2.1, Table 1), as can be seen in Fig. 4c. WCR vertical velocity data show that rising motion is stronger where the terrain ascends more steeply (Fig. 4b), indicating that the updrafts are terrain-driven, rather than buoyancy-driven. Yet these orographic updrafts are strong, estimated at up to ~3 m s^{-1} over the depth of the cloud. (1 m s^{-1} has been added to WCR mean vertical velocity values, to account for the hydrometeor fallspeEd.) Small-scale turbulent updrafts and downdrafts can be seen near the surface, confined mostly to the lowest 500 m AGL (Fig. 4b). These eddies mark the shear-driven boundary layer (Geerts et al., 2011). The turbulence mixes AgI nuclei into the boundary layer (Boe et al., 2014), and into cloud, in this and most other ASCII cases, since the cloud base (LCL) generally is below the level of the AgI generators (Table 1). The mean elevation of the main AgI generators over the SM (MB) is 2472 m (2869 m) MSL.

The upwind cloud top, at about −17 °C, is rich with cloud droplets, according to the high WCL backscatter power values delineating the cloud top (Fig. 4d). The black lines in Fig. 4c are tangential to the WCR dual-Doppler wind vectors. They represent hydrometeor streamlines if one assumes steady state conditions. These lines highlight hydrometeor ascent over the steeper sections of the upwind terrain, and plunging flow in the lee. Almost all snow falls on the upwind side (Fig. 4a). Some spill-over occurs on the lee, but the strong subsidence immediately behind the crest rapidly clears cloud liquid water (LW) (Fig. 4d). The plunging flow accelerates to ~20 m s^{-1} (Fig. 4c, Fig. 5b), and a shallow echo layer in the lee (advected snow or blowing snow) sublimates along the downhill slope (Fig. 4a). The fine-scale vertical-velocity fluctuations in this shallow layer (Fig. 4b) are due to mechanical turbulence, consistent with the strong winds. A hydraulic jump appears to be present near $x = 56$ km (Fig. 4b and c), lofting air at least up to flight level. Shallow stratiform clouds such as the one on 3 March 2012 are quite common in ASCII.

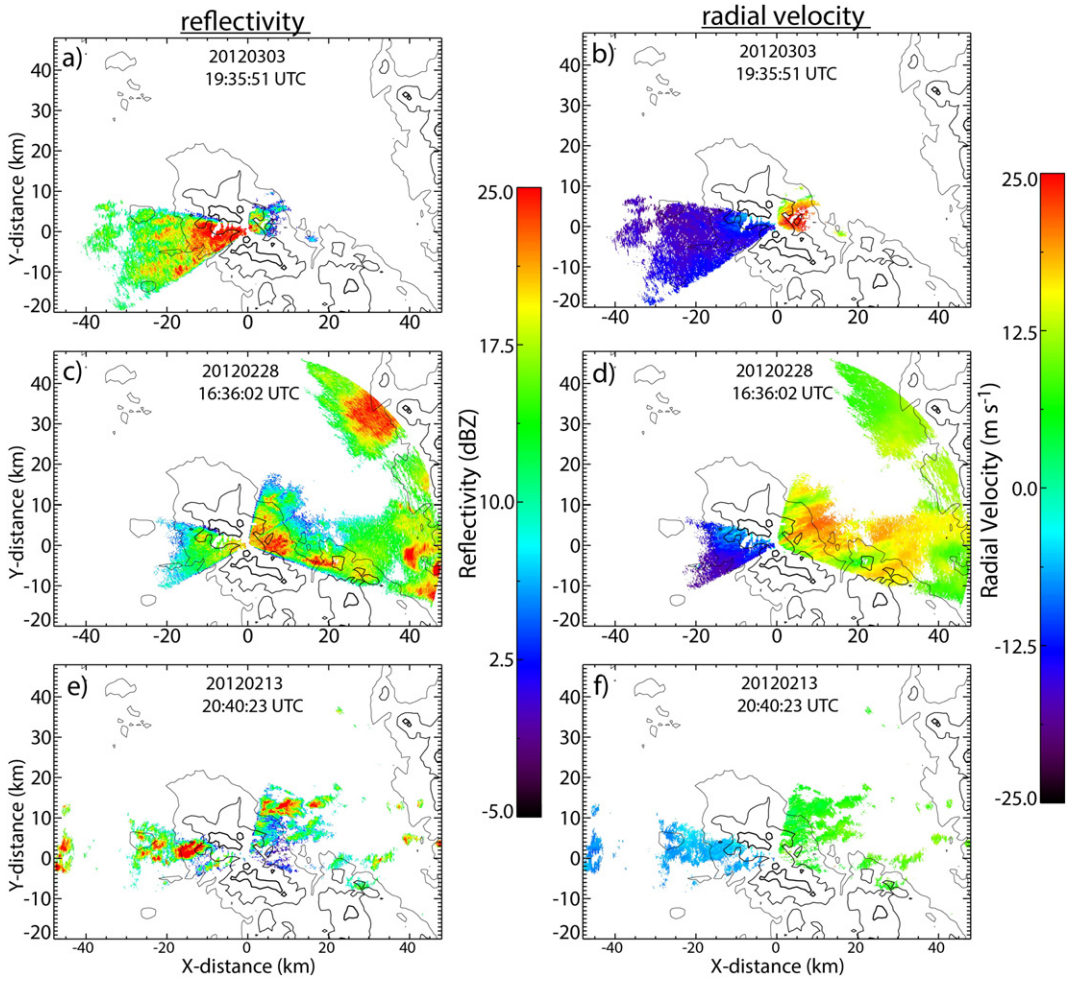

Fig. 5. DOW reflectivity (left panels) and radial velocity (right panels) for (top) 3 March 2012, (middle) 28 February 2012, and (bottom) 13 February 2012, at an elevation angle of 1°. The location of the DOW is shown in Fig. 1. Three terrain contours are shown, 2500, 2800, and 3100 m MSL (thin, medium, and bold black lines).

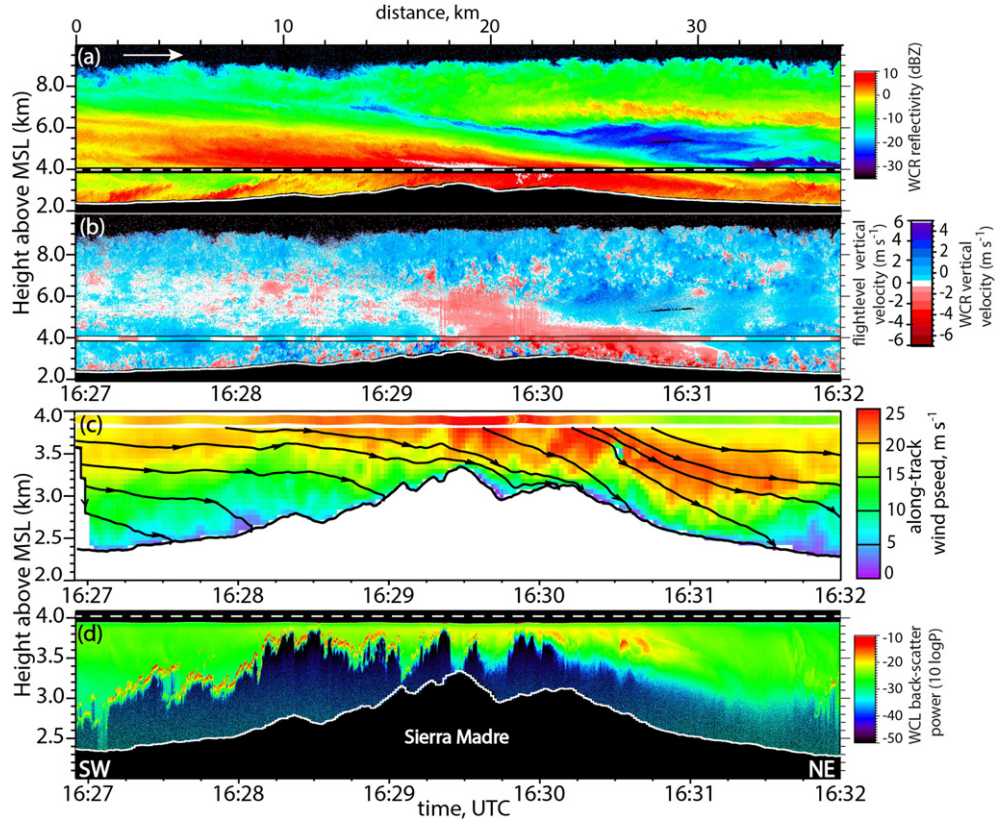

Fig. 6. As Fig. 4, but for an along-wind leg on 28 February 2012.

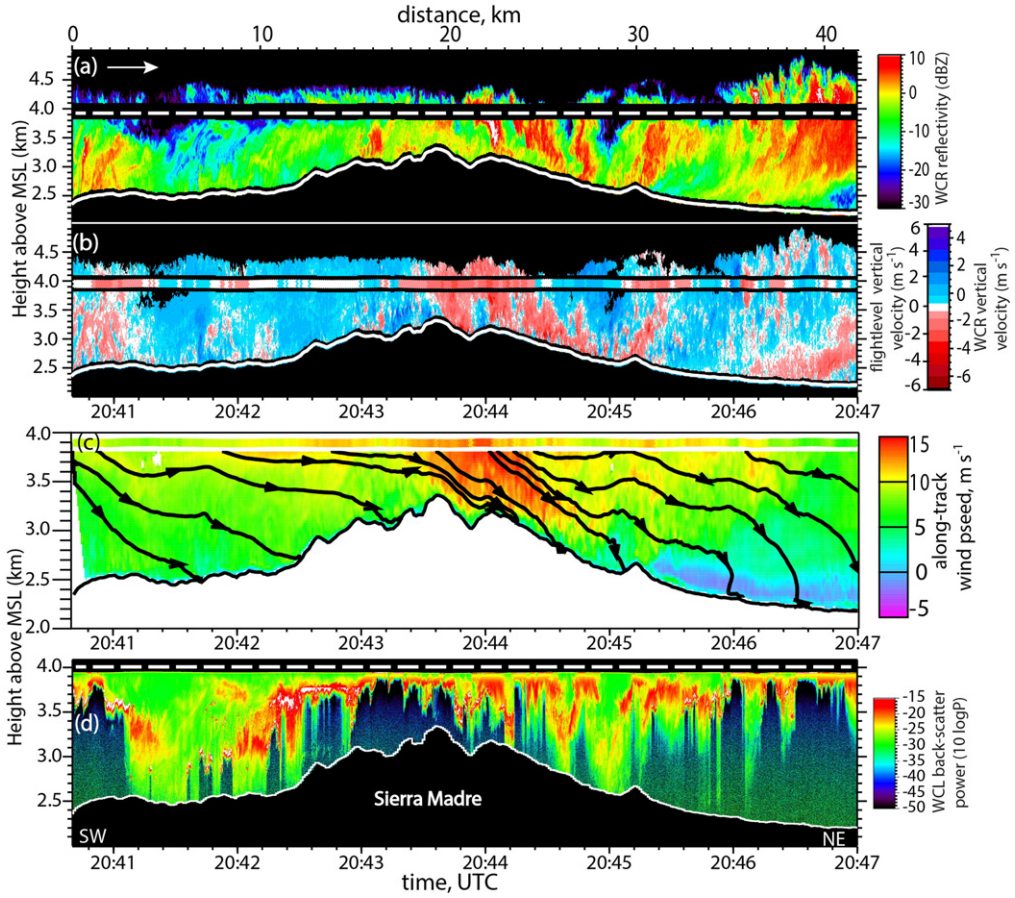

Fig. 7. As Fig. 4, but for an along-wind leg on 13 February 2012.

A second example, less common in ASCII, is a deep stratiform cloud observed on 28 February 2012 over the SM (Fig. 6). Upwind radiosonde data show a deep nearly moist-neutral cloud, with a few stable layers (Fig. 3b). The prevailing wind direction at low levels is southwesterly, i.e. roughly normal to the SM ridgeline. The WCR reflectivity transect shows widespread precipitation, heaviest near the mountain crest and in the immediate lee (Fig. 6a, Fig. 5c). Small generating cells and turbulent flow are present near the cloud top at ~9 km MSL (Fig. 6b). Shear-driven turbulence is present near the surface. Subsidence in the lee is confined to a shallow depth (Fig. 6b), resulting in cloud layer separation on the lee side (Fig. 6a). The upper level snow cloud is widespread, according to DOW data (not shown), but low-level precipitation largely vanishes in the valley east of the SM, and re-appears over the foothills of the MB (Fig. 5c). The low-level flow accelerates in the lee of the SM and decelerates again towards the MB range (Fig. 5d), consistent with linear wave theory over mountains. The larger upward and downward motions match with the flight level vertical velocity as well (Fig. 6b). The orographic ascent on the upwind side produces a shallow supercooled liquid cloud within the boundary layer (Fig. 6d), even though ice crystals fall from a homogeneously frozen upper cloud (cloud top temperature near −50 °C). The top of the shallow LW cloud is evident from the lidar backscatter power (Fig. 6d) below flight level. The disappearance of a thin line of very high WCL backscatter power across the crest indicates that most scatterers in the lee are ice crystals, not droplets. Much snow growth seems to occur in this region, mainly in echo cores that are tilted downshear (Fig. 6a, d).

4.2. Convective clouds

An example of shallow convective clouds, observed on 13 February 2012 over the SM, is shown in Fig. 7. The impact of glaciogenic seeding on these clouds is studied in Pokharel et al. (2014b). The low-level stability in this case is only slightly less than in the previous case (Fig. 3b): it is drier, especially above 4 km MSL, and closer to dry-adiabatic in the lowest few hundred meters (Fig. 3c). Equivalent potential temperature (θ_e) decreases with height at low levels, and the surface θ_e value is encountered only at 4.2 km MSL (Fig. 3d). As the air rises towards the SM, shallow convection emerges (Fig. 7a, Fig. 5e), with a cloud base well below crest level. (The LCL is about 2.4 km MSL, Table 1.) The wind is weak (~5 m s^{-1}, Table 1, and Fig. 5f). The lee acceleration is rather brief, and some near-surface counter-flow is present in the lee foothills ($x > 30$ km, Fig. 7c). The tops of the convective cells, near −18 °C, contain droplets, according to flight-level CDP data (not shown). Less LW appears present below flight level, as suggested by the lack of a well-defined WCL high power "fine" line in most areas (Fig. 7d). Convective updrafts (Fig. 7b) may temporarily loft hydrometeors, and many ice particles near the cloud top become rimed, according to flight-level CIP data (not shown). Convective cells persist on the leeward side (Fig. 7a, Fig. 5e), although much of the snow may sublimate.

These three transects show some common properties of the clouds sampled in ASCII. Firstly, these three and all other shallow cloud systems in ASCII contain supercooled LW on the upwind side, as

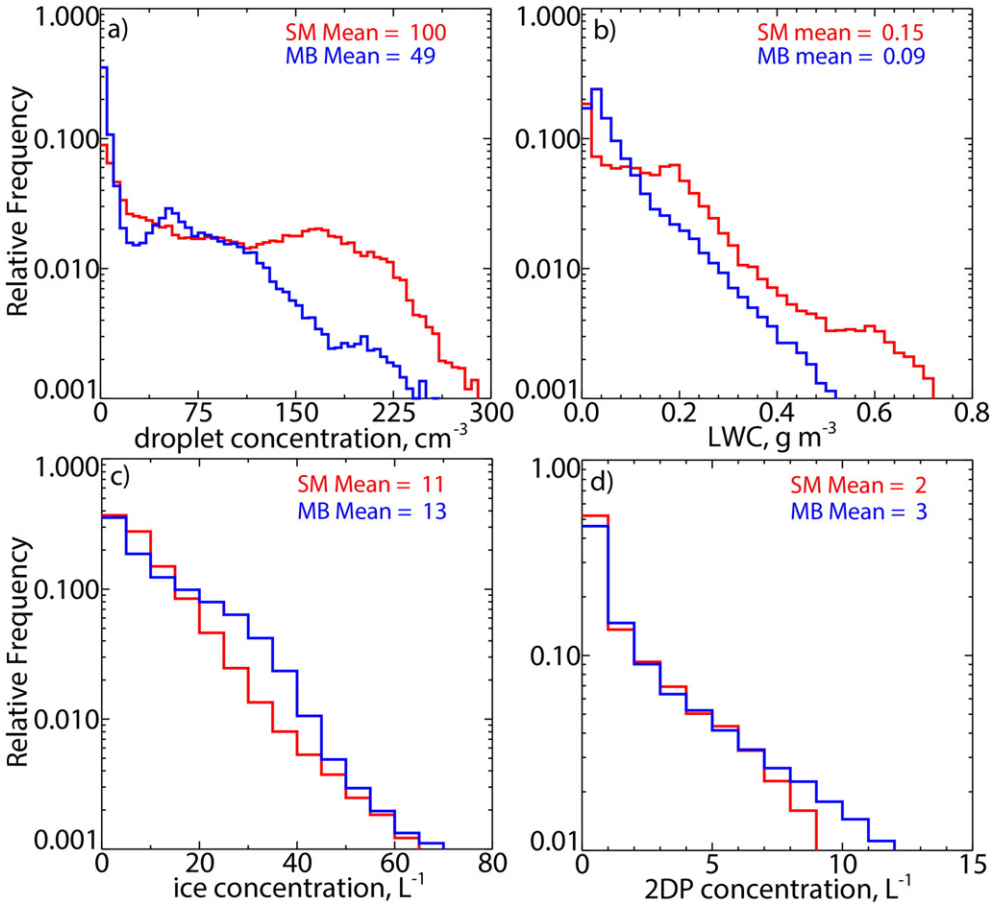

Fig. 8. Frequency distribution of cloud particle concentrations measured at flight level over the Sierra Madre (SM, red) and Medicine Bow (MB, blue). a) CDP-measured droplet concentration, b) CDP-measured liquid water content, c) CIP-measured concentration of ice particles (larger than 63 μm, and d) 2DP-measured particle concentration. The mean values are given in the upper right for both mountain ranges.

evident from WCL, flight-level data, and/or radiometer data. Secondly, snow falls naturally during all IOPs, in fact on all flight legs the WCR measures at least some echoes during NOSEED. And thirdly, all ASCII cases show a clear modulation of the flow, cloud, and precipitation across the mountain crest, with most clouds and precipitation contained near the mountain.

5. ASCII cloud microphysical characteristics: flight level data

The flight level in-situ data may be less useful to evaluate the impact of ground-based seeding, but they are useful to characterize the cloud microphysical properties. This is the case because clouds sampled at flight level in ASCII generally represent the same clouds as those seeded from the ground, because clouds generally are coupled to the surface, especially the shallow convective clouds. Also, the flight level generally is just 610 m above the local highest terrain (i.e., at ~4.0 km MSL in the SM and ~4.3 km in the MB range), although sometimes the flight level was raised because of airframe icing.

The LWC, droplet concentration, and ice particle concentration varies significantly between IOPs. A probability density function (PDF) of CDP droplet concentration, CDP LWC, and ice particle concentration according to the CIP and 2D-P probes is shown in Fig. 8, for almost all ASCII IOPs, i.e. 14 flights over the SM and 15 flights over the MB. Time segments are selected based on cloud penetrations, i.e. when the CDP droplet concentration exceeds 1 cm^{-3} and the CIP ice particle concentration (excluding the first two bins, i.e. particles larger than 63 μm) exceeds 1 L^{-1}. We exclude time segments when either of the two instruments did not perform properly, e.g. because of probe icing, and those shorter than 30 s (~2.5 km), to minimize the contribution of cloud margins. In most IOPs the time sections are >10 min long, within the ladder pattern shown in Fig. 1, but sometimes they are shorter, especially when the clouds are shallow and the aircraft is skimming the tops, as in Fig. 6. The data mostly come from legs #1–3, as subsidence over leg #5 (in the lee) and even leg #4 (over the crest) results in little cloud water. In situ cloud data are so limited in some IOPs, such as the one shown in Fig. 4, that the IOPs are excluded from the PDFs (Table 1). Therefore the PDFs in Fig. 8 contain some bias towards the deeper clouds and clouds with fewer large droplets (less icing). The PDFs include periods of AgI seeding, in order to fully capture the ASCII IOPs. Ground-based seeding clearly may affect cloud properties, but as mentioned above this is unlikely at flight level.

The CDP droplet concentration tends to be rather low, ~75 cm^{-3} on average. This average increases when the many instances of ice clouds, with just a few droplets cm^{-3}, are ignored, but the highest droplet concentration still is merely ~200 cm^{-3}. It is double in the clouds over the SM than those over the MB, which are sampled at a lower temperature. On average, the 700 mb temperature over the MB is about 5 K lower than over the SM (Table 1), plus the average flight level over the MB is ~300 m higher.

The LWC is generally low as well, ~0.1 g m^{-3} on average, and again generally higher in IOPs over the SM than in those over the MB. Only 1% of the cloud samples has LWC values exceeding 0.3 g m^{-3}. This is consistent with other observations in orographic clouds in the interior western USA (Section 1).

Most droplets are small, with a mode around 12 μm (8 μm) over the SM (MB). The composite droplet size distribution in Fig. 9a indicates that at most 12% of the droplets are larger than 20 μm, implying that growth by riming must be limited. Therefore most snow growth must occur by vapor deposition (and aggregation). Large droplets (mode ~ 35 μm) are encountered in one IOP over the SM [22 February 2012, the topic of a case study by Pokharel et al. (2015)]. Such drops caused the aircraft to abort the mission due to excessive airframe icing in another case over the SM (not included as an IOP).

The CIP ice particle concentration typically is ~10 L^{-1} in ASCII clouds (Fig. 8c). Ice particle concentrations >100 L^{-1} occasionally occur over both mountains, but in <1% of the ASCII clouds. Most of these particles are small, as the 2DP concentration is much smaller (Fig. 8d). In fact the CIP bin with the most particles is the smallest one (Fig. 9b). Both the CIP and the 2DP probes show a secondary peak in ice crystal concentration around 200–400 μm. Both the CIP and 2DP show higher ice concentrations and larger snowflakes over the SM, which implies a typically higher snow mass and precipitation rate over the SM. This is consistent with the higher mean radar reflectivity and snowfall rate in IOPs over the SM, as shown in Part II.

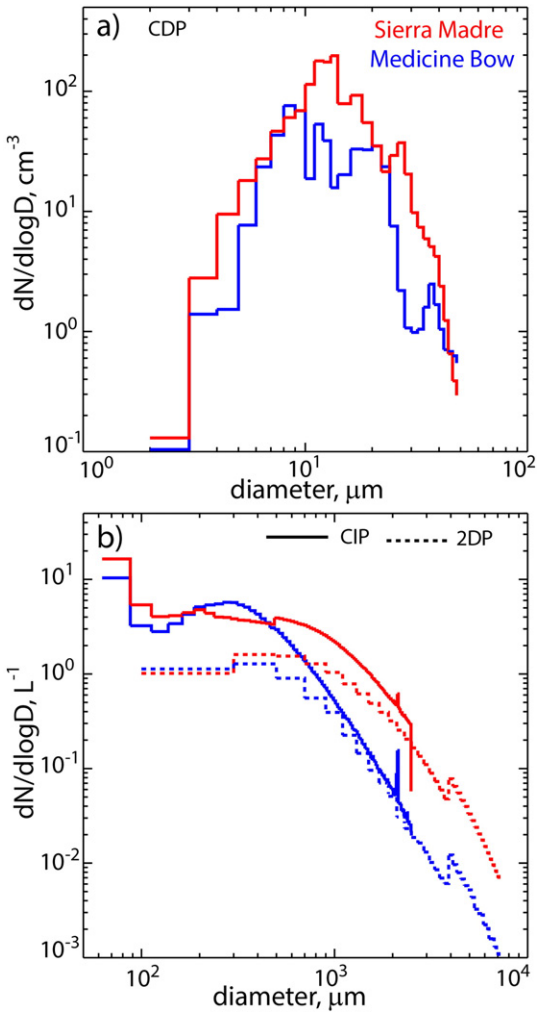

Fig. 9. Droplet (CDP) and ice particle (CIP and 2D-P) size distributions measured at flight level during ASCII over the MB (red) and the SM (blue) ranges. The data come from all UWKA cloud penetrations in all IOPs.

6. Spatial decorrelation rate of precipitation

The variability of precipitation at even very small spatial and temporal scales remains the biggest challenge in isolating an unambiguous impact of seeding (Garstang et al., 2005). Natural trends in intensity of orographic precipitation over periods of a few hours tend to be significant even if wind, temperature, and basic storm characteristics are rather steady during the IOP, which includes a SEED and a NOSEED period. In ASCII and in other studies, the attribution of change to seeding is based on the comparison of changes in a target region compared to those in a control region. The latter is either upwind of the ground-based AgI generators (called upwind control) or along the target mountain range far from the possible seeding plume (called lateral control). Parallel measurements in this region only serve as a control when

precipitation in target and control regions are strongly correlated. This section analyses this correlation for different instruments including WCR, DOW and snow gauges. Ideally, a long-term record from a dense network is available to build solid spatial correlations of precipitation over relevant time scales. Our analysis is limited to the small number of winter storms sampled in ASCII, as none of the probes operated outside the ASCII field phase.

For the WCR, we have 21 IOPs with good data, consisting of a small upwind control region (leg 1) and a large downwind target region (legs 2–5) (Fig. 1). The flight legs were not long enough to allow partitioning legs 2–5 in a lateral control region and a target region. For the DOW, we can use all 10 IOPs listed in Table 1 for upwind control, but only 5 IOPs for lateral control, i.e. only those cases for which the wind direction was suitable to define a lateral control region. The exact definition of the DOW target, upwind and lateral control regions depends on wind direction, and is given in Part II. Their approximate location is shown in Fig. 10b. And for the surface snow gauges, good data are available from both target and lateral control gauges (location shown in Fig. 1) for 17 periods. The correlation analysis is focused on the NOSEED part of the IOPs to avoid contamination of the correlation by seeding.

We use the leg-mean reflectivity below 0.5 km AGL as a proxy for near-surface precipitation for the WCR data, and correlate the values for leg 1 against those for the downwind legs (Fig. 10c). For the DOW, we use the mean reflectivity below <1.5 km AGL at any grid point to estimate the near-surface precipitation rate for DOW, using the relationship $Z = 100R^{1.5}$ (Z in mm^6 m^{-3}, R in mm h^{-1}). These estimates then are spatially correlated (Fig. 10a–b). And for the surface snow gauges, correlations are based on the cumulative precipitation during the NOSEED period (Fig. 10d).

The correlation coefficient of the DOW mean precipitation rate during the ~two-hour long NOSEED periods is 0.95 both for the 10 DOW upwind control IOPs and the 5 DOW lateral control IOPs; it is 0.90 for the combined 15 pairs (Fig. 10a). The spatial autocorrelation of the precipitation rate based on the DOW reflectivity data for all 10 IOPs during their NOSEED periods is mapped in Fig. 10b relative to SM04, a point located between the control and target regions. The region of low-level DOW data is geographically limited because the DOW was located in a

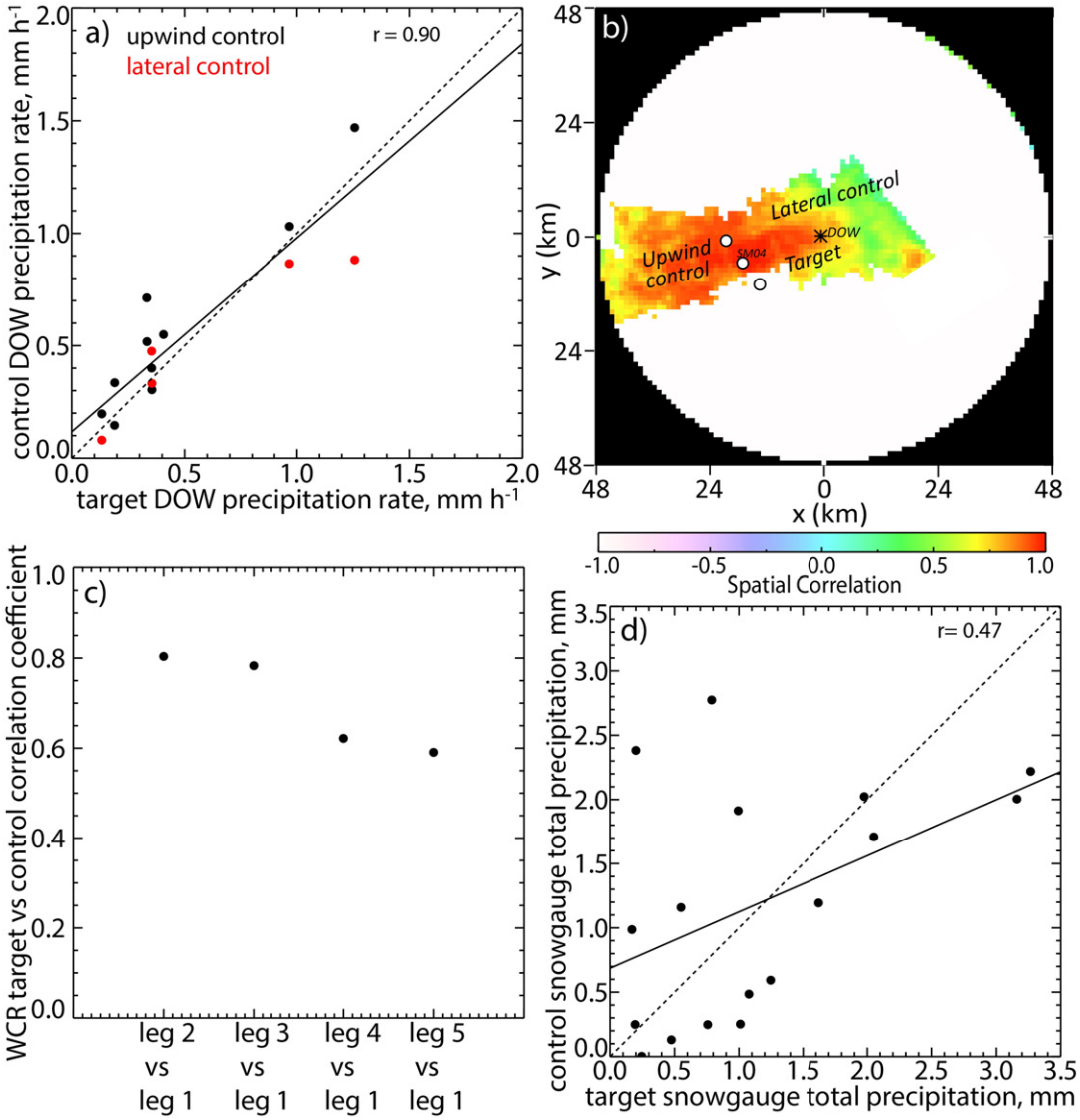

Fig. 10. Spatial correlation of precipitation or reflectivity measurements across the SM and MB mountains. a) Scatterplot of DOW-estimated mean precipitation rate within control and target regions, for all 10 cases using an upwind control region, and for 5 cases using a lateral control region. b) Composite spatial autocorrelation of hourly precipitation rate for 10 cases with DOW data, relative to SM04. c) Correlation of mean WCR low-level reflectivity between leg 1 and the downwind legs, based on 21 IOPs; d) scatterplot of snow gauge precipitation for 17 IOPs with snow gauge data over the two mountain ranges. In a) and c), the solid and dotted lines are the best-fit linear relationship to the points and 1:1 lines, respectively.

terrain saddle (Fig. 1) with good low-level coverage to the west and NE, but poor coverage to the NW and SE because of terrain blockage. Precipitation in the upwind control region (the foothills of the SM) correlates well with that in the target area (the SM mountain), at least the part of the target area upwind of the crest. The lateral control area (high terrain to the N and S) correlates slightly better, on average, but is smaller. The lee area correlates poorly with windward area (<0.5), consistent with the lower correlation of WCR reflectivity between leg 1 and leg 5, which is in the lee (Fig. 10c). The WCR reflectivity along the upwind control leg correlates better with that along the nearby target legs, but the correlation coefficient with leg 1 remains above 0.5 even for leg 5 (Fig. 10c). Note that the WCR spatial correlation is not based on simultaneous measurements, unlike that for the DOW. The correlation between target gauges and lateral control gauges is rather low (0.47) (Fig. 10d), probably because the latter are more distant (Fig. 1). The DOW-based correlation coefficients are more meaningful because the base of comparison is spatially-averaged precipitation (over an area of ~400 km^2), rather than point measurements.

In short, the target and control regions appear to be reasonably correlated, especially for the DOW.

7. Conclusions

This two-part study examines the impact of ground-based AgI seeding on snow growth in wintertime orographic clouds observed in southern Wyoming between 2008 and 2013 as part of the ASCII project. Part I describes the campaigns and conditions encountered during the ASCII IOPs. IOPs were called based on general criteria of suitability for glaciogenic seeding (LW presence, temperature, and wind direction), as well as predicted storm steadiness. The low-level wind is generally strong (14 m s^{-1} on average), and the stability in the upwind valley relatively low, such that the bulk Froude number is large (>1) in most cases, ensuring flow over the mountain, towards the target region. The clouds sampled in the ASCII IOPs cover a broad range of temperatures and SLW content, but generally are rather shallow (2.1 km deep on average), have little liquid water (LWP < 0.3 mm in most cases) and produce light precipitation (<1 mm h^{-1} in most cases). However, all clouds have some liquid water and produce snowfall naturally before seeding, with a typical ice particle concentration of ~10 L^{-1} at flight level. Nearly two thirds of the ASCII IOPs have only stratiform clouds; clouds in the remainder are entirely convective, or have convection embedded in stratiform clouds. The droplets sampled at flight level are mostly smaller in size, therefore most snow growth must occur by vapor deposition even before seeding. There is a rather strong correlation between precipitation measurements in the proposed target and control regions, according to different instruments, especially the DOW, whose target and control regions are relatively large.

The impact of AgI seeding on snow growth in these clouds is explored using radar and particle probe data in Part II.

Acknowledgements

The ASCII campaign is funded by the National Science Foundation grant AGS-1058426. This work also received funding from the Wyoming Water Development Commission grant 1001552C and the United States Geological Survey grant 10000628S, under the auspices of the University of Wyoming Water Research Program. The operation of the AgI generators, the upstream MRR, and the microwave radiometer was supported by the WWMPP, which is funded by the State of Wyoming and managed by Barry Lawrence. We thank the crews of the UWKA and the DOW for working under often harsh conditions, Katja Friedrich for collecting and sharing MRR and Parsivel data from Battle Pass, Dan Breed for the MRR data collected at Ladder Livestock ranch, Arlen Huggins for the trace analysis of snow samples collected at Battle Pass, and Bob Rauber for relevant insights and background

References

Boe, B.A., Heimback, A., Krauss, T.W., Xue, L., Chu, X., McPartland, J.T., 2014. The dispersion of silver iodide particles from ground-based generators over complex terrain. Part I: observations with acoustic ice nucleus counters. J. Appl. Meteor. Climatol. 53, 1325–1341.
Breed, D., Rasmussen, R., Weeks, C., Boe, B., Deshler, T., 2014. Evaluating winter orographic cloud seeding: design of the Wyoming Weather Modification Pilot Project (WWMPP). J. Appl. Meteor. Climatol. 53, 282–299.
Chu, X., Xue, L., Geerts, B., Rasmussen, R., Breed, D., 2014. A case study of radar observations and WRF LES simulations of the impact of ground-based glaciogenic seeding on orographic clouds and precipitation: part I: observations and model validations. J. Appl. Meteor. Climat. 53, 2264–2286.
Cooper, W.A., Saunders, C.P.R., 1980. Winter storms over the San Juan Mountains. Part II: microphysical processes. J. Appl. Meteor. 19, 927–941.
Cooper, W.A., Vali, G., 1981. The origin of ice in mountain cap clouds. J. Atmos. Sci. 38, 1244–1259.
DeMott, P.J., 1997. Report to North Dakota Atmospheric Resource Board and Weather Modification Incorporated on Tests of the Ice Nucleating Ability of Aerosols Produced by the Lohse Airborne Generator. Dept. Atmos. Sci., Colorado State Univ., Report, Fort Collins, CO 15 pp.
DeMott, P.J., Finnegan, W.G., Grant, L.O., 1983. An application of chemical kinetic theory and methodololgy to characterize the ice nucleating properties of aerosols used for weather modification. J. Climate Appl. Meteor. 22, 1190–1203.
DeMott, P.J., Prennia, A.J., Liu, X., Kreidenweis, S.M., Petters, M.D., Twohy, C.H., Richardson, M.S., Eidhammer, T., Rogers, D.C., 2010. Predicting global atmospheric ice nuclei distributions and their impacts on climate. Proc. Nat. Acad. Sci. http://dx.doi.org/10.1073/pnas.0910818107.
Dery, S.J., Yau, M.K., 1999. A climatology of adverse winter-type weather events. J. Geophys. Res. 104, 16657–16672.
Garstang, M., Bruintjes, R., Serafin, R., Orville, H., Boe, B., Cotton, W., Warburton, J., 2005. Finding common ground. Bull. Amer. Meteor. Soc. 86, 647–655.
Geerts, B., Damiani, R., Haimov, S., 2006. Fine-scale vertical structure of a cold front as revealed by airborne radar. Mon. Wea. Rev. 134, 251–272.
Geerts, B., Miao, Q., Yang, Y., 2011. Boundary-layer turbulence and orographic precipitation growth in cold clouds: evidence from profiling airborne radar data. J. Atmos. Sci. 68, 2344–2365.
Geerts, B., Pokharel, B., Friedrich, K., Breed, D., Rasmussen, R., Yang, Y., Miao, Q., Haimov, S., Boe, B., Kalina, E., 2013. The AgI seeding cloud impact investigation (ASCII) campaign 2012: overview and preliminary results. J. Weather Mod. 45, 24–43.
Geerts, B., Yang, Y., Rasmussen, R., Haimov, S., Pokharel, B., 2015a. Snow growth and transport patterns in orographic storms as estimated from airborne vertical-plane dual-Doppler radar data. Mon. Wea. Rev. 143, 644–665.
Geerts, B., Pokharel, B., Kristovich, D.A.R., 2015b. Blowing snow as a natural glaciogenic cloud seeding mechanism. Mon. Wea. Rev. 143, 5017–5033.
Givati, A., Rosenfeld, D., 2005. Separation between cloud-seeding and air-pollution effects. J. Appl. Meteor. 44, 1298–1314. http://dx.doi.org/10.1175/JAM2276.1.
Grant, L.O., Elliott, R.E., 1974. The cloud seeding temperature window. J. Appl. Meteor. 13, 355–363.
Harris-Hobbs, R.L., Cooper, W.A., 1987. Field evidence supporting quantitative predictions of secondary ice production rates. J. Appl. Meteor. 44, 1071–1082.
Hobbs, P.V., 1975. The nature of winter clouds and precipitation in the Cascade Mountains and their modification by artificial seeding. Part I: natural conditions. J. Appl. Meteor. 14, 783–804.
Houze Jr., R.A., 2014. Cloud Dynamics. Second Edition Academic press (573 pp).
Huggins, A.W., 1995. Mobile microwave radiometer observations: spatial characteristics of supercooled cloud water and cloud seeding implications. J. Appl. Meteor. 34, 432–446.
Jing, X., Geerts, B., 2015. Dual-polarization radar data analysis of the impact of ground-based glaciogenic seeding on winter orographic clouds. Part II: convective clouds. J. Appl. Meteor. Climat. 54, 2099–2117.
Jing, X., Geerts, B., Friedrich, K., Pokharel, B., 2015. Dual-polarization radar data analysis of the impact of ground-based glaciogenic seeding on winter orographic clouds. Part I: mostly stratiform clouds. J. Appl. Meteor. Climatol. 54, 1944–1969.
Long, A.B., Carter, E.J., 1996. Australian Winter Mountain storm clouds: precipitation augmentation potential. J. Appl. Meteor. 35, 1457–1464.
Plummer, D.M., McFarquhar, G.M., Rauber, R.M., Jewett, B.F., Leon, D.C., 2014. Structure and statistical analysis of the microphysical properties of generating cells in the comma head region of continental winter cyclones. J. Atmos. Sci. 71, 4181–4203.
Pokharel, B., Geerts, B., 2014. The impact of glaciogenic seeding on snowfall from shallow orographic clouds over the Medicine Bow Mountains in Wyoming. J. Wea. Mod. 46, 8–28.
Pokharel, B., Geerts, B., Jing, X., 2014a. The impact of ground-based glaciogenic seeding on orographic clouds and precipitation: a multi-sensor case study. J. Appl. Meteor. Climatol. 53, 890–909.
Pokharel, B., Geerts, B., Jing, X., Friedrich, K., Aikins, J., Breed, D., Rasmussen, R., Huggins, A., 2014b. The impact of ground-based glaciogenic seeding on orographic clouds and precipitation: a multi-sensor case study of shallow precipitating orographic cumuli. Atmos. Res. 147-148, 162–181.
Pokharel, B., Geerts, B., Jing, X., 2015. The impact of ground-based glaciogenic seeding on clouds and precipitation over mountains: a case study of shallow orographic cloud with large supercooled droplets. J. Geophys. Res. 120, 6056–6079.
Pokharel, B., Geerts, B., Jing, X., Friedrich, K., Ikeda, K., Rasmussen, R., 2017. A multi-sensor study of the impact of ground-based glaciogenic seeding on clouds and precipitation over mountains in Wyoming. Part II: seeding impact analysis. Atmos. Res. 183, 42–57.
Politovich, M.K., Vali, G., 1983. Observations of liquid water in orographic clouds over Elk Mountain. J. Atmos. Sci. 40, 1300–1312. http://dx.doi.org/10.1175/1520-0469(1983)040.

Pruppacher, H.R., Klett, J.D., 1997. Microphysics of Clouds and Precipitation. Kluwer Academic (954 pp.).
Rauber, R.M., 1987. Characteristics of cloud ice and precipitation during wintertime storms over the mountains of Northern Colorado. J. Climate Appl. Meteor. 26, 488–524.
Rauber, R.M., Grant, L.O., 1987. Supercooled liquid water structure of a shallow orographic cloud system in southern Utah. J. Climate Appl. Meteor. 26, 208–215.
Rauber, R.M., Tokay, A., 1991. An explanation for the existence of supercooled water at the top of cold clouds. J. Atmos. Sci. 48, 1005–1023.
Rogers, D.C., Vali, G., 1987. Ice crystal production by mountain surfaces. J. Climate Appl.
Sassen, K., Huggins, A.W., Long, A.B., Snider, J.B., Meitín, R.J., 1990. Investigations of a Winter Mountain storm in Utah. Part II: mesoscale structure, supercooled liquid water development, and precipitation processes. J. Atmos. Sci. 47, 1323–1350.
Schaefer, V.J., 1946. The production of ice crystals in a cloud of supercooled water droplets. Science 104, 457–459.
Wang, P.K., Ji, W., 2000. Collision efficiencies of ice crystals at low-intermediate Reynolds numbers colliding with supercooled cloud droplets: a numerical study. J. Atmos. Sci. 57, 1001–1009.
Wang, Z., French, J., Vali, G., Wechsler, P., Haimov, S., Rodi, A., Deng, M., Leon, D., Snider, J., Peng, L., Pazmany, A.L., 2012. Single aircraft integration of remote sensing and in situ sampling for the study of cloud microphysics and dynamics. Bull. Amer. Meteor. Soc. 93, 653–668.
Xue, L., Chu, X., Rasmussen, R., Breed, D., Boe, B., Geerts, B., 2014. The dispersion of silver iodide particles from ground-based generators over complex terrain. Part II: WRF large-eddy simulations vs. observations. J. Appl. Meteor. Climatol. 53, 1342–1361.